crystals

MDPI

Article

Effects of Buffer Layer on Structural Properties of Nonpolar (11$\bar{2}$0)-Plane GaN Film

Jianguo Zhao [1,2,*], Boyan Suo [1], Ru Xu [1], Tao Tao [2], Zhe Zhuang [3], Bin Liu [2,*], Xiong Zhang [4] and Jianhua Chang [1,*]

[1] School of Electronics and Information Engineering, Nanjing University of Information Science and Technology, Nanjing 210044, China
[2] School of Electronic Science and Engineering, Nanjing University, Nanjing 210023, China
[3] School of integrated Circuits, Nanjing University, Suzhou 215163, China
[4] Advanced Photonics Center, Southeast University, Nanjing 210096, China
* Correspondence: zhaojg@nuist.edu.cn (J.Z.); bliu@nju.edu.cn (B.L.); jianhuachang@nuist.edu.cn (J.C.)

Abstract: Nonpolar (11$\bar{2}$0) *a*-plane GaN films were grown on semipolar (1$\bar{1}$02) *r*-plane sapphire substrates using various buffer layers within a low-pressure metal organic chemical vapor deposition system. The structural properties of nonpolar *a*-plane GaN films were intensively investigated by X-ray diffraction and Raman spectra measurements. A set of buffer layers were adopted from a GaN layer to a composite layer containing a multiple AlN layers and a gradually varied-Al-content AlGaN layer, the full width at half maximum of the X-ray rocking curves measured along the [0001] and [10$\bar{1}$0] directions of *a*-plane GaN were reduced by 35% and 37%, respectively. It was also found that the basal-plane stacking faults (BSFs) density can be effectively reduced by the heterogeneous interface introduced together with the composite buffer layer. An order of magnitude reduction in BSFs density, as low as 2.95×10^4 cm^{-1}, and a pit-free surface morphology were achieved for the *a*-plane GaN film grown with the composite buffer layer, which is promising for the development of nonpolar GaN-based devices in the future.

Keywords: buffer layer; structural properties; nonpolar GaN

Citation: Zhao, J.; Suo, B.; Xu, R.; Tao, T.; Zhuang, Z.; Liu, B.; Zhang, X.; Chang, J. Effects of Buffer Layer on Structural Properties of Nonpolar (11$\bar{2}$0)-Plane GaN Film. *Crystals* **2023**, *13*, 1145. https://doi.org/10.3390/cryst13071145

Academic Editor: Francisco M. Morales

Received: 7 July 2023
Revised: 17 July 2023
Accepted: 19 July 2023
Published: 22 July 2023

1. Introduction

The light emitting and optoelectronic devices fabricated based on III-nitrides offer a wide spectral range varying from near-infrared (InN) to deep ultraviolet (AlN) [1–3]. Remarkable progress has been reported on the research of InGaN-based green and red light-emitting diodes (LEDs) [4–7], AlGaN-based deep ultraviolet (DUV) LEDs [8,9], GaN-based ultraviolet photodetectors [10], and AlGaN-based solar-blind photodetectors [11]. High-bandwidth light communication could be achieved based on the above visible light and ultraviolet LEDs [9,12]. Accompanied with these achievements, both the efficiency and the modulation bandwidth of III-nitride-based LEDs were limited by the built-in electric-field-induced quantum-confined Stark effect (QCSE) [13–15]. Although the QCSE can be suppressed/eliminated by growing semipolar/nonpolar GaN-based structures [16], the epitaxial growth of semipolar/nonpolar III-nitride structures was still a great challenge [17,18]. Therefore, the development of semipolar/nonpolar structures has lagged behind the development of polar structures.

Recently, high-bandwidth semipolar (20$\bar{2}$1)-plane GaN-based LED has been widely reported for visible-light communication [19,20] due to the successful fabrication of high-quality commercial semipolar (20$\bar{2}$1)-plane GaN templates. Meanwhile, a bandwidth of 540 MHz for (11$\bar{2}$2)-plane semipolar green LEDs had been demonstrated by growing an (11$\bar{2}$2)-plane GaN template whose crystalline quality was similar to or close to that of polar GaN [21]. The research on nonpolar AlGaN-based ultraviolet light-related structures [22,23] and InGaN-based visible light-related structures [24,25] has been investigated, but there is

still much room for the investigation of devices based on nonpolar III-nitrides. Obviously, the successful fabrication of nonpolar GaN templates is the basis for the realization of nonpolar GaN-based devices. Although free-standing nonpolar GaN templates of comparable quality to polar GaN are currently available, they are cut at a specific angle from ultra-thick *c*-plane GaN, are typically only a few millimeters (~5 mm) width, and are difficult to commercialize.

Similar to the studies such as the SiN_x interlayer [26] and the NH_3 pulsed-flow growth technology [27] on the conventional *c*-plane polar III-nitride structures, various technologies such as buffer layers [28,29], in situ SiN_x interlayers [30], growth interruption [31], and substrate nitridation [32] have been extensively investigated to acquire nonpolar GaN films. The blocking effect of the SiN_x insertion layer on BSFs was verified by the TEM measurements reported by M.J. Kappers et al. [33]. It was found that a nonpolar GaN film with a pit-free and smooth surface could be achieved by using a composite buffer layer containing a low-temperature-grown AlN layer sandwiched in between two high-temperature-grown AlN layers [28]. R. Hao et al. reported that the defects in nonpolar *a*-plane GaN film could be reduced using either a SiN_x interlayer or a direct-growth technology (without a nucleation layer) [34]. In addition, a composite buffer layer consisting of a low-temperature-grown AlN layer, a low-temperature-grown pulsed AlN layer, and a low-temperature-grown AlGaN layer improved the crystal quality of nonpolar *a*-plane GaN film [35]. Recently, $(11\bar{2}0)$-plane nonpolar GaN film was successfully grown on a (0001)-plane sapphire substrate using pulsed laser deposition (PLD) technology [36]. It was reported that the crystalline quality of nonpolar GaN could be improved by introducing a patterned SiO_2 layer [37]. However, the introduction of secondary epitaxy processes or growth techniques that are not entirely based on the metal organic chemical vapor deposition (MOCVD) system is detrimental to commercialization. Therefore, epitaxial structures grown in a single process by using pure MOCVD technology are usually pursued.

In this study, several nonpolar $(11\bar{2}0)$-plane GaN films were grown on *r*-plane sapphire substrates by using a low-pressure MOCVD system. The buffer layer was modified to investigate the effect of the buffer layer on the structural properties of nonpolar $(11\bar{2}0)$-plane GaN films. It was found that a composite buffer layer containing multiple AlN layers and a gradually varied-Al-content AlGaN layer was effective in improving the crystal quality and suppressing the basal-plane stacking faults (BSFs) density. The FWHM of XRCs measured along the [0001] and $[10\bar{1}0]$ directions of *a*-plane GaN was reduced by 35% and 37%, respectively, and a BSFs density as low as 2.95×10^4 cm^{-1} was achieved using the optimized composite buffer layer.

2. Experiment

In this study, a low-pressure MOCVD system was used to grow the nonpolar $(11\bar{2}0)$ *a*-plane GaN films on the semipolar $(1\bar{1}02)$ *r*-plane sapphire substrates. This MOCVD system is a domestically manufactured 2-inch monolithic system with a vertically coupled chamber. The chamber pressure was maintained at 40 Torr throughout the growth process. The precursors for Al, Ga, and N elements were trimethylaluminum (TMAl), trimethylgallium (TMGa), and ammonia (NH_3), respectively, while the carrier gas of the MOCVD system was hydrogen (H_2). Five nonpolar GaN samples, labeled as A–E, were grown based on various buffer layer structures to investigate the effects of the buffer layer on the structural properties of nonpolar GaN films. The epitaxial structures of the nonpolar GaN films are shown in Figure 1. Specifically, the buffer layer of sample A contained a low-temperature (650 °C) grown GaN nucleation (LT-GaN) layer and a high-temperature (1030 °C) grown GaN (HT-GaN) layer. The growth duration time, NH_3 flow rate, and TMGa flow rate of the LT-GaN layer were 7 min, 112 mmol/min, and 15.6 µmol/min, respectively, while these parameters were 15 min, 80 mmol/min, and 38.9 µmol/min, respectively, for the growth of the HT-GaN layer. For sample B, its buffer layer contained a low-temperature (720 °C) grown AlN layer (LT-AlN) and a high-temperature (1090 °C) grown AlN (HT-AlN) layer, respectively. Correspondingly, the growth duration time, NH_3 flow rate, and TMAl

flow rate of the LT-AlN layer were 7 min, 62.5 mmol/min, and 3.5 µmol/min, respectively, while these parameters were 30 min, 44.6 mmol/min, and 23.2 µmol/min, respectively, for the growth of the HT-AlN layer. The buffer layer of sample C was a multiple AlN layer, which was identical to our previous report [30]. Specifically, it contained a 720 °C grown LT-AlN layer sandwiched in between two 1050 °C grown HT-AlN layers. The NH_3 and TMAl flow rates were 22.3 mmol/min, and 8.7 µmol/min for all the three AlN layers, respectively, and the growth duration time was 3, 4.5, and 7.5 min for the first HT-AlN layer, the LT-AlN layer, and the second HT-AlN layer, respectively. An AlGaN layer was grown on the multiple AlN layers of sample C to constitute the buffer layer of sample D. The growth temperature, duration time, NH_3 flow rate, TMAl flow rate, and TMGa flow rate were 1090 °C, 15 min, 112 mmol/min, 14.7 µmol/min, and 32.4 µmol/min, respectively. In other words, the gas phase Al content of this AlGaN layer was ~0.31. For structure E, the fixed Al content AlGaN layer was replaced by a varied-Al-content AlGaN layer whose gas phase Al content was gradually decreased from 0.7 to 0.07 from the beginning to the end, as a strain-relaxation layer. The growth temperature and NH_3 flow rate were fixed at 1090 °C and 84.8 mmol/min, respectively, while the flow rate of TMAl and TMGa was varied over the growth time. As shown in Figure 2, the flow rate of TMAl was started at 29.0 µmol/min, and gradually decreased linearly over time to 2.9 µmol/min, while the flow rate of TMGa was started at 12.3 µmol/min, and gradually increased linearly over time to 38.1 µmol/min. During this growth period, the flow rate of TMAl and TMGa was kept constant, so that the V/III ratio was maintained at ~2000.

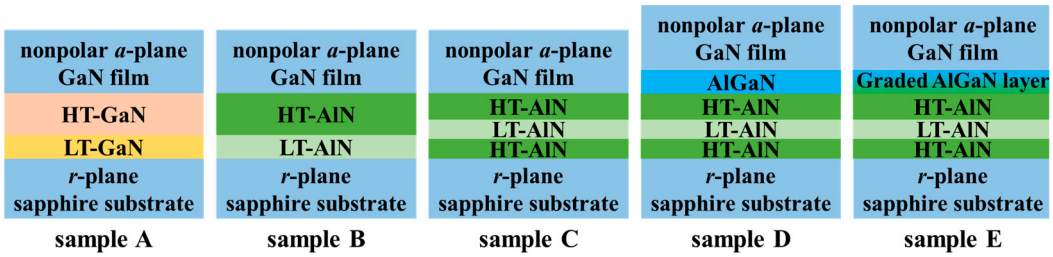

Figure 1. The schematic diagram of the epitaxial layer structures of the samples A–E.

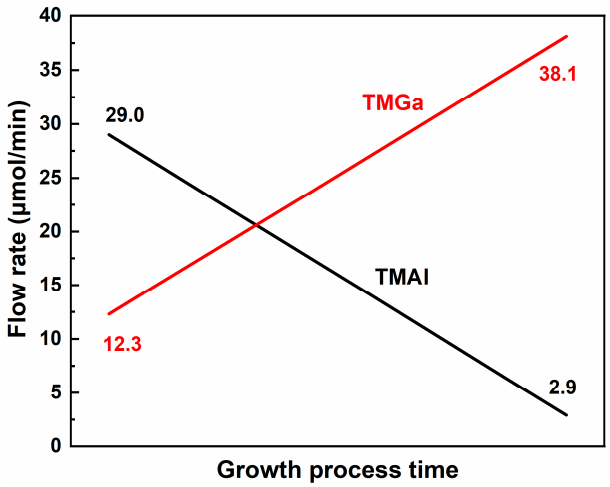

Figure 2. The flow rate chart of TMAl and TMGa in the growth of varied-Al-content AlGaN layer.

After growing the buffer layer, an unintentionally doped nonpolar *a*-plane GaN film was grown on top of the buffer layer at 1030 °C. During this growth process, the flow rates of NH_3 and TMGa were 67.0 mmol/min and 68.1 µmol/min, respectively, resulting in a growth rate of 1.8 µm/h, as verified in our previous work [30]. In this study, a 1.2 µm thick *a*-plane GaN film was grown in 40 min. After growing all the nonpolar *a*-plane GaN samples, the crystalline quality was characterized by measuring the X-ray rocking curves (XRCs) of

(11$\bar{2}$0)-plane GaN along the in-plane *c*- and *m*-directions. The BSFs density was calculated based on the modified Williamson–Hall analysis by measuring the XRCs of (h0$\bar{h}$0)-planes GaN. Meanwhile, the in-plane strains along the *c*- and *m*-directions of nonpolar GaN were analyzed by measuring Raman spectra at RT under the x(-,-)$\bar{x}$ configuration. The surface morphology was observed with an optical microscope at 500X.

3. Results and Discussions

The X-ray diffraction (XRD) 2θ-ω scanning curves for samples A–E are shown in Figure 3a. The two main peaks located at 2θ = 52.56 and 57.76° were diffracted from the (2$\bar{2}$04)-plane of sapphire and (11$\bar{2}$0)-plane of GaN, as labeled in Figure 3a. These XRD 2θ-ω scanning curves indicated the successful growth of nonpolar *a*-plane GaN film. For samples B–E, a relatively weak peak located at 59.35° can be observed. These peaks were diffracted from the (11$\bar{2}$0)-plane AlN. On the other hand, a distinct "shoulder peak" can be distinguished between the XRD peaks of GaN and AlN, which was diffracted from the inserted AlGaN layers for samples D and E. The relatively broad diffraction peak of AlGaN in sample E was due to the fact that this layer was grown with a gradually decreasing gas phase Al content. Meanwhile, the XRCs were scanned along the in-plane [0001] *c*-direction and [10$\bar{1}$0] *m*-direction for each sample, and their corresponding full width at half maximum (FWHM), denoted as C_{FWHM} and M_{FWHM}, respectively, were determined by a single Gaussian function fitting and are illustrated in Figure 3b. These relatively large FWHM indicated that the crystalline quality of nonpolar GaN was inferior to that of conventional polar GaN, which was the main reason for the slow development of nonpolar GaN-based structures compared to their polar counterpart [17]. The fact that C_{FWHM} was much smaller than M_{FWHM} indicated the anisotropy in the crystalline quality of nonpolar GaN due to the anisotropy in lattice mismatch between the GaN epilayer and the sapphire substrate along the *c*- and *m*-directions [38], which is a typical feature of nonpolar GaN [18,30]. In fact, the in-plane *c*- and *m*-directions of the nonpolar *a*-plane III-nitrides epitaxially grown on an *r*-plane sapphire substrate are parallel to the [$\bar{1}$101] and [11$\bar{2}$0] directions of the sapphire substrate, respectively [38]. Here, the lattice mismatch is defined as follows:

$$\delta = \frac{a_{sub} - a_{epi}}{a_{epi}} \times 100\%, \quad (1)$$

where a_{sub} and a_{epi} are the lattice lengths along a specific direction of the substrate and epitaxial layers, respectively. Along the *c*-direction of nonpolar *a*-plane III-nitrides, the lattice lengths for GaN and AlN are 4.982 and 5.185 Å, respectively, i.e., their lattice constant c. The lattice length for [$\bar{1}$101] sapphire is 5.09 Å. In contrast, along the *m*-direction of nonpolar *a*-plane III-nitrides, the lattice lengths for GaN and AlN are 5.39 and 5.52 Å, respectively, which is $\sqrt{3}$ times their lattice constant a. The lattice length for [11$\bar{2}$0] sapphire is 4.71 Å [39]. Thus, the lattice mismatch along the two directions between the grown nonpolar III-nitrides and sapphire substrate can be calculated and are summarized in Table 1.

Table 1. The lattice mismatch between the nonpolar *a*-plane III-nitrides and the semipolar *r*-plane sapphire substrate.

III-Nitrides	Along *c*-Direction of III-Nitrides	Along *m*-Direction of III-Nitrides
GaN	−1.83%	−14.73%
AlN	2.17%	−12.62%

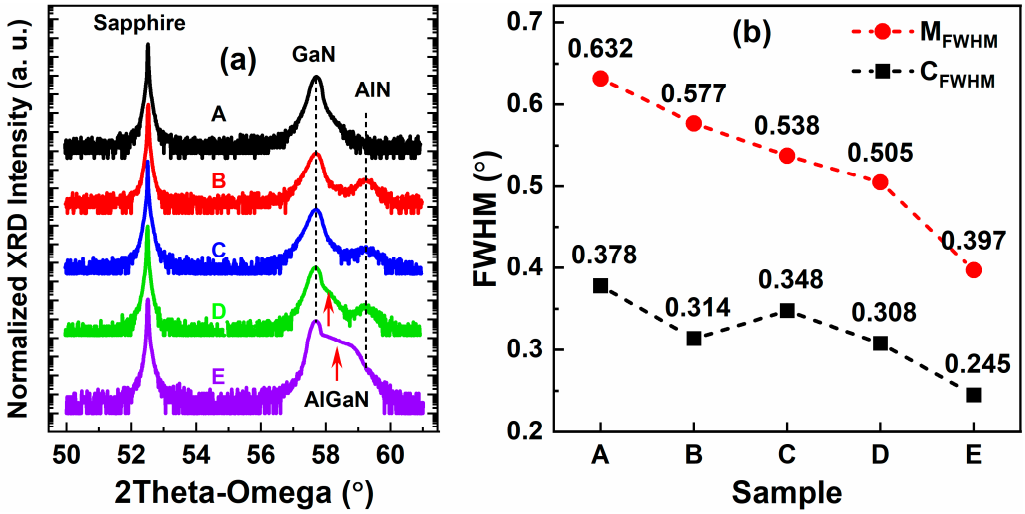

Figure 3. The XRD 2θ-ω curves of samples A–E (**a**) and the FWHM of the (11$\bar{2}$0) GaN XRCs measured along *c*- and *m*-directions (**b**). The arrows in (**a**) indicate the diffraction peaks of AlGaN layers.

The FWHM of the XRCs was found to vary with respect to the buffer layers. Among them, the crystalline quality of samples B and C contacted with the AlN buffer layers was slightly better than that of sample A containing only a GaN buffer layer. The improved quality was inferred due to the introduction of tensile stress along the *c*-direction induced by the AlN buffer layer, which partially compensated the compressive stress in the upper GaN layer [40]. Therefore, due to the extra stress relaxation effects of the AlGaN layer, the crystal quality of samples D and E was further improved, and the best crystal quality was achieved for sample E, which contained a gradually varied-Al-content AlGaN layer. Specifically, the C_{FWHM} and M_{FWHM} for sample E were reduced by 35% and 37%, respectively, compared to sample A, due to the introduction of the optimized buffer layer. The reduced C_{FWHM} and M_{FWHM} indicated the improved crystalline quality and the reduced structural defects, which will improve the performance of future devices.

The BSFs in nonpolar *a*-plane III-nitrides stacked along the *c*-direction and propagated from bottom to top along the growth direction, the *a*-direction, and acted as a leaky, non-radiative recombination center. Thus, the BSFs are usually considered to be the major defects in nonpolar III-nitrides. To investigate the effects of different buffer layers on the BSFs density, the modified Williamson–Hall analysis [41] was introduced to calculate the BSFs density in all the five *a*-plane nonpolar GaN samples. First, the XRCs of the (10$\bar{1}$0)- and (20$\bar{2}$0)-planes of each nonpolar GaN sample were measured along the *c*-direction. Then, the BSFs density was derived based on the flow equation:

$$\Delta\omega_{\text{measured}} = \Delta\omega_{\text{mosaic}} + \frac{\lambda}{2Lsin(\theta_{hkl})}. \quad (2)$$

Here, $1/L$ is the BSFs density, which can be calculated by a linear fitting based on the FWHM values of the XRCs diffracted from the (10$\bar{1}$0)- and (20$\bar{2}$0)-planes of GaN. The XRD ω-2θ scanning curves of the (10$\bar{1}$0)- and (20$\bar{2}$0)-planes for sample A are shown in Figure 4a as representative. Figure 4b demonstrates the modified Williamson–Hall plots for the five samples based on the measured XRCs. The intercept of the corresponding fitted line in Figure 4b is the calculated BSFs density for each sample, and their values are plotted in Figure 4c.

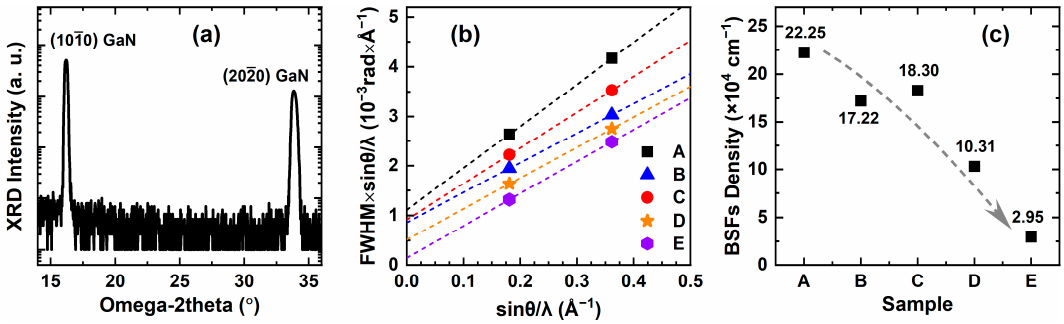

Figure 4. The ω-2θ XRD curve scanned along *c*-direction for (10$\bar{1}$0)- and (20$\bar{2}$0)-planes of sample A (**a**). The modified Williamson–Hall plots (**b**), and the calculated BSFs density (**c**) for the five samples.

It can be seen from Figure 4c that the BSFs density in sample A was the highest among the five samples, while the BSFs density in samples B and C was slightly decreased after the use of the AlN buffer layer. After the introduction of the AlGaN layer, the BSFs density in sample D was significantly reduced by about 40% compared to samples B and C, and by 54% compared to sample A. When the gradually varied-Al-content AlGaN layer was introduced for sample E, the BSFs density was further reduced by 71% compared to sample D, as low as 2.95×10^4 cm^{-1}, and an order of magnitude reduction was achieved compared to sample A. This density was reduced by 64% compared to our previous work (8.13×10^4 cm^{-1}) on the growth of nonpolar *a*-plane GaN using an in situ SiN_x interlayer [42], and reduced by 56% compared to the result (6.7×10^4 cm^{-1}) reported by J. Liang et al. on the growth of *a*-plane GaN on lattice-matched $LaAlO_3$ substrates [43]. In fact, the evolution trend of the BSFs density of the five samples was basically consistent with that of the FWHM of the XRCs, as shown in Figure 3b. In general, the BSFs, which were formed at the initial stage of growth and propagated along the growth direction, can be partially blocked by heterogeneous interfaces. The decrease in the BSFs density in samples B and C compared to sample A could be attributed to the blocking of BSFs by the AlN buffer/upper GaN interface. For sample D, two additional interfaces, the AlN/AlGaN and AlGaN/GaN interfaces, were added based on sample C, both of which can have the effect of blocking the propagation of BSFs. The varied-Al-content AlGaN layer in sample E corresponded to many heterogeneous interfaces, exerting a continuous blocking effect on the propagation of BSFs. Therefore, a significant (about an order of magnitude) decrease in the BSFs density was achieved for sample E compared to sample A, proving that the gradually varied-Al-content AlGaN layer played a major role in suppressing the BSFs density.

The Raman spectra measured at room temperature under a configuration of x(-,-)$\bar{x}$ for samples A–E are plotted in Figure 5a. The three Raman peaks marked with * were sapphire peaks [44], and the right peak marked with # was the overlapping peak of sapphire and GaN E_1(LO) [44,45]. The three Raman peaks located between 500 and 600 cm^{-1} from left to right were the GaN A_1 (TO), E_1 (TO), and E_2 (high) mode-related Raman peaks, respectively, as marked in Figure 5a. The in-plane strains of nonpolar GaN films can be calculated based on the Raman peak positions of the E_1 (TO) and E_2 (high) modes. In fact, the mathematical relationship between the strains along different GaN in-plane directions and the Raman shift of the corresponding mode is represented by the following equation:

$$\Delta\omega_\lambda = a_\lambda\left(1 - \frac{c_{12}}{c_{11}}\right)\varepsilon_{yy} + \left(b_\lambda - a_\lambda\frac{c_{13}}{c_{11}}\right)\varepsilon_{zz} + c_\lambda|\varepsilon_{xx} - \varepsilon_{yy}|. \quad (3)$$

Here, $\Delta\omega_\lambda$ represents the Raman shift of a particular mode, c_{11}, c_{12}, and c_{13} are the elastic stiffness constants for GaN [46], a_λ, b_λ, and c_λ represent the corresponding phonon deformation potentials for the particular mode [38,47], and ε_{xx}, ε_{yy}, and ε_{zz} are the strains along the GaN $[11\bar{2}0]$, $[1\bar{1}00]$, and [0001] directions, respectively [32,48]. The peak positions for the E_1(TO) and E_2(high) modes of strain-free GaN were assigned to be 558.8 and 567.6 cm^{-1}, respectively. The measured peak positions of the E_1(TO) and E_2(high) modes

of samples A–E are summarized in Table 2. Then, two equations for the strains along different directions can be obtained by substituting the Raman shifts of the E_1 (TO), and E_2 (high) modes into the above equation. Meanwhile, the strain along the growth direction is assumed to be zero based on the linear elasticity theory, while the strains, ε_{xx}, ε_{yy}, and ε_{zz} are subject to the following expressions [38]:

$$\varepsilon_{yy} = -\frac{c_{11}}{c_{12}}\varepsilon_{xx} - \frac{c_{13}}{c_{12}}\varepsilon_{zz}. \quad (4)$$

Then, a ternary system of equations was constructed and the in-plane strains, ε_{zz} and ε_{yy}, were obtained by solving the above equations. The solved in-plane strains of the five nonpolar GaN are demonstrated in Figure 5b.

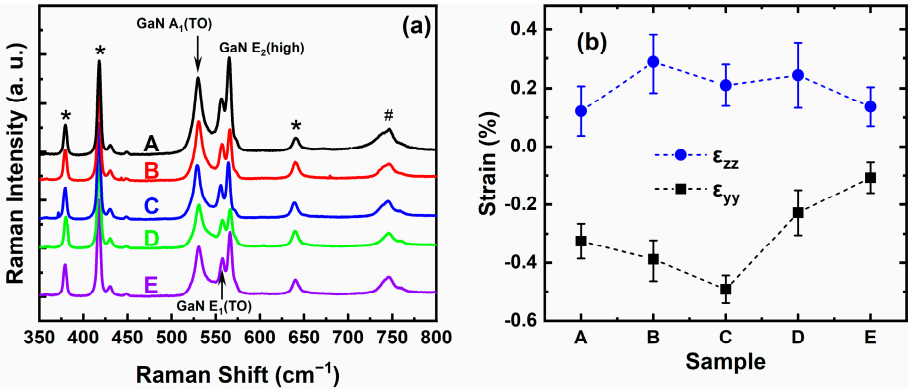

Figure 5. The Raman spectra measured from 350 to 800 cm^{-1} (**a**) and the calculated in-plane strains (**b**) for samples A–E. The three Raman peaks marked with * were sapphire peaks and the right peak marked with # was the overlapping peak of sapphire and GaN E_1(LO).

Table 2. The measured peak positions of E_1(TO) and E_2(high) modes of nonpolar GaN samples A–E.

Raman Mode	Sample A	Sample B	Sample C	Sample D	Sample E
E_1(TO), cm^{-1}	556.11	556.40	554.92	557.04	558.45
E_2(high), cm^{-1}	565.13	565.79	564.13	566.29	567.55

The in-plane strains in sample A grown on GaN buffer were significantly reduced compared to those in samples B and C grown on AlN buffer. It can be concluded that the in-plane strains in sample A were partially released by the formation of BSFs at the initial stage of growth. For samples B and C, the strain along the *c*-direction was partially compensated by the tensile strain introduced along with the AlN buffer layer. In this case, the residual strain in the GaN layer was reduced, and therefore the proportion of strains released by formatting the BSFs was synchronously reduced. As a result, the in-plane strains in samples B and C were larger, and the BSFs density was smaller than those in sample A.

When an additional layer of AlGaN was introduced for samples D and E, the in-plane strains were slightly reduced due to the lattice mismatch between the top GaN and bottom AlN being transited by the inserted AlGaN layer. In other words, due to the lattice lengths along a certain direction of the AlGaN being between AlN and GaN, the lattice mismatch of the GaN film for samples D and E was between the upper GaN layer and the lower AlGaN layer, while the lattice mismatch of the GaN film for samples B and C was between the upper GaN layer and the lower AlN layer. This means that when the AlGaN was introduced, the lattice mismatch between the GaN film and the lower layer was actually reduced. On the other hand, the propagation of the BSFs could be partially blocked by the additional interfaces introduced along with the AlGaN layer. Thus, both the FWHM of the XRCs and the BSFs density were improved with the introduction of the AlGaN layer.

Obviously, the AlGaN layer whose Al content varied gradually from 0.7 to 0.07 in sample E produced a better transition effect on the lattice mismatch, so that sample E achieved a smaller in-plane strains compared to sample D.

As shown in Figure 6, the directional stripes distributed on the surface parallel to the in-plane *c*-direction are due to the fact that the in-plane growth rate along the *c*-direction was higher than that along the *m*-direction [49], and are the typical surface morphology of $(11\bar{2}0)$-plane GaN-based materials [25]. It can be seen from Figure 6 that relatively more triangular pits were distributed on the surface of samples B and C, while the distribution on the surface of sample C was less, and samples A and E achieved a pit-free surface morphology. The formation of these triangular pits is usually related to the strains in nonpolar GaN. The pit-free surface of samples A and E was inferred because the strains were partially released by the formation of BSFs for sample A, and were compensated by the introduced composite buffer layer for sample E. Therefore, the composite buffer layer introduced in this study can improve the crystal quality, reduce the BSFs density, and form a pit-free surface in the growth of nonpolar *a*-plane GaN films.

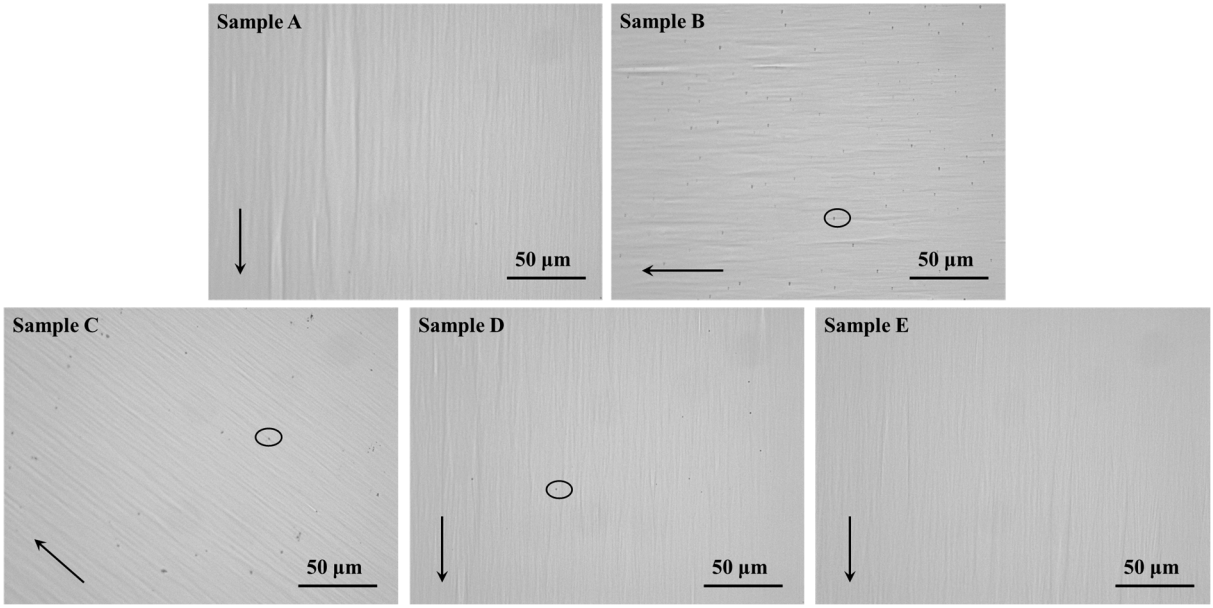

Figure 6. The surface images of all the five nonpolar GaN samples. The arrows and circles indicated the *c*-direction and the superficial triangular pits of nonpolar *a*-plane GaN, respectively.

4. Conclusions

The effects of buffer layers on the structural properties of nonpolar $(11\bar{2}0)$ *a*-plane GaN films have been intensively investigated. The in-plane strains can be suppressed by optimizing the buffer layers, resulting in improved crystalline quality. An AlGaN layer was introduced to compensate for the in-plane strains in the *a*-plane GaN due to the usage of AlN buffer layer. It was calculated that the C_{FWHM} and M_{FWHM} were reduced by 35% and 37%, respectively, compared to a reference sample using GaN as the buffer layer. Meanwhile, the BSFs density can be effectively reduced by the heterogeneous interface introduced together with the buffer layers. A BSFs density as low as 2.95×10^4 cm^{-1}, an order of magnitude lower than that of the reference sample, and a pit-free surface morphology were achieved for the sample grown with a composite buffer layer containing multiple AlN and gradually varied-Al-content AlGaN layers, providing promising insights for the development of nonpolar devices in the future.

Author Contributions: Conceptualization, methodology, software, resources, data curation, writing-original draft, review and editing, funding acquisition, J.Z.; Data curation, B.S. and R.X.; Resources, writing—review and editing, supervision, funding acquisition, T.T., Z.Z. and B.L.; Supervision, X.Z. and J.C. All authors have read and agreed to the published version of the manuscript.

Funding: This research was funded by the National Key R&D Program of China (2021YFB3601000, 2021YFB3601002), the National Natural Science Foundation of China (Grant Nos. 62204121, 61974062, 62274083), and the China Postdoctoral Science Foundation (Grant No. 2020M671441).

Data Availability Statement: The data that support the findings of this study are available within the article.

Conflicts of Interest: The authors declare no conflict of interest.

References

1. Liu, B.; Chen, D.; Lu, H.; Tao, T.; Zhuang, Z.; Shao, Z.; Xu, W.; Ge, H.; Zhi, T.; Ren, F.; et al. Hybrid Light Emitters and UV Solar-Blind Avalanche Photodiodes based on III-Nitride Semiconductors. *Adv. Mater.* **2020**, *32*, 1904354. [CrossRef] [PubMed]
2. Jiang, B.; Zhu, S.; Ren, L.; Shi, L.; Zhang, X. Simultaneous ultraviolet, visible, and near-infrared continuous-wave lasing in a rare-earth-doped microcavity. *Adv. Photonics* **2022**, *4*, 046003. [CrossRef]
3. Meng, W.; Xu, F.; Yu, Z.; Tao, T.; Shao, L.; Liu, L.; Li, T.; Wen, K.; Wang, J.; He, L.; et al. Three-dimensional monolithic micro-LED display driven by atomically thin transistor matrix. *Nat. Nanotechnol.* **2021**, *16*, 1231. [CrossRef]
4. Zhang, S.; Zhang, J.; Gao, J.; Wang, X.; Zheng, C.; Zhang, M.; Wu, X.; Xu, L.; Ding, J.; Quan, Z.; et al. Efficient emission of InGaN-based light-emitting diodes: Toward orange and red. *Photonics Res* **2020**, *8*, 1671–1675. [CrossRef]
5. Bi, Z.; Lenrick, F.; Colvin, J.; Gustafsson, A.; Hultin, O.; Nowzari, A.; Lu, T.; Wallenberg, R.; Timm, R.; Mikkelsen, A.; et al. InGaN Platelets: Synthesis and Applications toward Green and Red Light-Emitting Diodes. *Nano Lett.* **2019**, *19*, 2832–2839. [CrossRef]
6. Iida, D.; Zhuang, Z.; Kirilenko, P.; Velazquez-Rizo, M.; Najmi, M.A.; Ohkawa, K. 633-nm InGaN-based red LEDs grown on thick underlying GaN layers with reduced in-plane residual stress. *Appl. Phys. Lett.* **2020**, *116*, 162101. [CrossRef]
7. Lu, S.; Li, J.; Huang, K.; Liu, G.; Zhou, Y.; Cai, D.; Zhang, R.; Kang, J. Designs of InGaN micro-LED structure for improving quantum efficiency at low current density. *Nanoscale Res. Lett.* **2021**, *16*, 99. [CrossRef] [PubMed]
8. Sun, H.; Mitra, S.; Subedi, R.C.; Zhang, Y.; Guo, W.; Ye, J.; Shakfa, M.K.; Ng, T.K.; Ooi, B.S.; Roqan, I.S.; et al. Unambiguously Enhanced Ultraviolet Luminescence of AlGaN Wavy Quantum Well Structures Grown on Large Misoriented Sapphire Substrate. *Adv. Funct. Mater.* **2019**, *29*, 1905445. [CrossRef]
9. Yu, H.; Memon, M.H.; Jia, H.; Ding, Y.; Xiao, S.; Liu, X.; Kang, Y.; Wang, D.; Zhang, H.; Fang, S.; et al. Deep-Ultraviolet LEDs Incorporated with SiO_2-Based Microcavities Toward High-Speed Ultraviolet Light Communication. *Adv. Opt. Mater.* **2022**, *10*, 2201738. [CrossRef]
10. Yang, Y.; Wang, W.; Zheng, Y.; You, J.; Huang, S.; Wu, K.; Kong, D.; Luo, Z.; Chen, H.; Li, G. Defect effect on the performance of nonpolar GaN-based ultraviolet photodetectors. *Appl. Phys. Lett.* **2021**, *118*, 053501. [CrossRef]
11. Cai, Q.; You, H.; Guo, H.; Wang, J.; Liu, B.; Xie, Z.; Chen, D.; Lu, H.; Zheng, Y.; Zhang, R. Progress on AlGaN-based solar-blind ultraviolet photodetectors and focal plane arrays. *Light Sci. Appl.* **2021**, *10*, 94. [CrossRef]
12. Chang, Y.H.; Hsu, T.C.; Liou, F.J.; Chow, C.W.; Liu, Y.; Kuo, H.C.; Yeh, C.H.; Yang, P.H. High-bandwidth InGaN/GaN semipolar micro-LED acting as a fast photodetector for visible light communications. *Opt. Express* **2021**, *29*, 37245–37252. [CrossRef]
13. Bernardini, F.; Fiorentini, V.; Vanderbilt, D. Spontaneous polarization and piezoelectric constants of III-V nitrides. *Phys. Rev. B* **1997**, *56*, R10024. [CrossRef]
14. Fiorentini, V.; Bernardini, F.; Della Sala, F.; Di Carlo, A.; Lugli, P. Effects of macroscopic polarization in III-V nitride multiple quantum wells. *Phys. Rev. B* **1999**, *60*, 8849–8858. [CrossRef]
15. Liu, X.; Lin, R.; Chen, H.; Zhang, S.; Qian, Z.; Zhou, G.; Chen, X.; Zhou, X.; Zheng, L.; Liu, R.; et al. High-bandwidth InGaN self-powered detector arrays toward MIMO visible light communication based on micro-LED arrays. *ACS Photonics* **2019**, *6*, 3186–3195. [CrossRef]
16. Waltereit, P.; Brandt, O.; Trampert, A.; Grahn, H.; Menniger, J.; Ramsteiner, M.; Reiche, M.; Ploog, K. Nitride semiconductors free of electrostatic fields for efficient white light-emitting diodes. *Nature* **2000**, *406*, 865–868. [CrossRef]
17. Monavarian, M.; Rashidi, A.; Feezell, D. A Decade of Nonpolar and Semipolar III-Nitrides: A Review of Successes and Challenges. *Phys. Status Solidi A* **2018**, *216*, 1800628. [CrossRef]
18. Zhao, J.; Zhang, X.; Dai, Q.; Wang, N.; Wu, Z.; Wang, S.; Cui, Y. Defects reduction in *a*-plane AlGaN epi-layers grown on r-plane sapphire substrates by metal organic chemical vapor deposition. *Appl. Phys. Express* **2017**, *10*, 011002. [CrossRef]
19. Li, H.; Li, P.; Zhang, H.; Chow, Y.C.; Wong, M.S.; Pinna, S.; Klamkin, J.; Speck, J.S.; Nakamura, S.; DenBaars, S.P. Electrically driven, polarized, phosphor-free white semipolar (20-21) InGaN light-emitting diodes grown on semipolar bulk GaN substrate. *Opt. Express* **2020**, *28*, 13569–13575. [CrossRef]
20. Chen, S.-W.H.; Huang, Y.-M.; Chang, Y.-H.; Lin, Y.; Liou, F.-J.; Hsu, Y.-C.; Song, J.; Choi, J.; Chow, C.-W.; Lin, C.-C.; et al. High-Bandwidth Green Semipolar (20–21) InGaN/GaN Micro Light-Emitting Diodes for Visible Light Communication. *ACS Photonics* **2020**, *7*, 2228–2235. [CrossRef]

21. Haggar, J.I.; Cai, Y.; Ghataora, S.S.; Smith, R.M.; Bai, J.; Wang, T. High Modulation Bandwidth of Semipolar (11-22) InGaN/GaN LEDs with Long Wavelength Emission. *ACS Appl. Electron. Mater.* **2020**, *2*, 2363–2368. [CrossRef] [PubMed]
22. Zhao, J.; Zhang, X.; He, J.; Chen, S.; Wu, Z.; Fan, A.; Dai, Q.; Feng, Z.C.; Cui, Y. High Internal Quantum Efficiency of Nonpolar a-Plane AlGaN-Based Multiple Quantum Wells Grown on r-Plane Sapphire Substrate. *ACS Photonics* **2018**, *5*, 1903–1906. [CrossRef]
23. Zhao, J.; Pan, J.; Liu, B.; Tao, T.; Chen, D.; Long, X.; Feng, Z.C.; Chang, J. Improved Optical Properties of Nonpolar AlGaN-Based Multiple Quantum Wells Emitting at 280 nm. *IEEE Photonics J.* **2021**, *13*, 2300107. [CrossRef]
24. Ketzer, F.A.; Horenburg, P.; Henning, P.; Korn, E.R.; Bremers, H.; Rossow, U.; Hangleiter, A. Control of optical polarization properties by manipulation of anisotropic strain in nonpolar m-plane GaInN/GaN quantum wells. *Appl. Phys. Lett.* **2019**, *114*, 052101. [CrossRef]
25. Zhao, J.; Chen, K.; Gong, M.; Hu, W.; Liu, B.; Tao, T.; Yan, Y.; Xie, Z.; Li, Y.; Chang, J.; et al. Epitaxial growth and characteristics of nonpolar *a*-plane InGaN films with blue-green-red emission and entire In content range. *Chin. Phys. Lett.* **2022**, *39*, 048101. [CrossRef]
26. Benzarti, Z.; Sekrafi, T.; Bougrioua, Z.; Khalfallah, A.; El Jani, B. Effect of SiN Treatment on Optical Properties of InxGa1−x N/GaN MQW Blue LEDs. *J. Electron. Mater.* **2017**, *46*, 4312–4320. [CrossRef]
27. Hirayama, H.; Maeda, N.; Fujikawa, S.; Toyoda, S.; Kamata, N. Recent progress and future prospects of AlGaN-based high-efficiency deep-ultraviolet light-emitting diodes. *Jpn. J. Appl. Phys.* **2014**, *53*, 100209. [CrossRef]
28. Chiang, C.H.; Chen, K.M.; Wu, Y.H.; Yeh, Y.S.; Lee, W.I.; Chen, J.F.; Lin, K.L.; Hsiao, Y.L.; Huang, W.C.; Chang, E.Y. Nonpolar *a*-plane GaN grown on r-plane sapphire using multilayer AlN buffer by metalorganic chemical vapor deposition. *Appl. Surf. Sci.* **2011**, *257*, 2415–2418. [CrossRef]
29. Xu, P.; Zhou, Z. Silicon-based optoelectronics for general-purpose matrix computation: A review. *Adv. Photonics* **2022**, *4*, 044001. [CrossRef]
30. Zhao, J.; Zhang, X.; Wu, Z.; Dai, Q.; Wang, N.; He, J.; Chen, S.; Feng, Z.C.; Cui, Y. Reduction in crystalline quality anisotropy and strain for non-polar *a*-plane GaN epi-layers with nano-scale island-like SiN_x interlayer. *J. Alloys Compd.* **2017**, *729*, 992–996. [CrossRef]
31. Song, K.-M.; Kang, D.-H.; Shin, C.-S.; Kim, H.; Kim, J.-M. Improvement of crystal quality of nonpolar *a*-plane GaN by in-situ surface modification. *Mater. Lett.* **2013**, *93*, 356–359. [CrossRef]
32. Zhang, J.; Tian, W.; Wu, F.; Wan, Q.; Wang, Z.; Zhang, J.; Li, Y.; Dai, J.; Fang, Y.; Wu, Z.; et al. The effects of substrate nitridation on the growth of nonpolar *a*-plane GaN on r-plane sapphire by metalorganic chemical vapor deposition. *Appl. Surf. Sci.* **2014**, *307*, 525–532. [CrossRef]
33. Kappers, M.J.; Hollander, J.L.; Johnston, C.F.; McAleese, C.; Sridhara Rao, D.V.; Sanchez, A.M.; Humphreys, C.J.; Badcock, T.J.; Dawson, P. Properties of non-polar *a*-plane GaN/AlGaN quantum wells. *J. Cryst. Growth* **2008**, *310*, 4983–4986. [CrossRef]
34. Hao, R.; Kappers, M.J.; Moram, M.A.; Humphreys, C.J. Defect reduction processes in heteroepitaxial non-polar *a*-plane GaN films. *J. Cryst. Growth* **2011**, *337*, 81–86. [CrossRef]
35. Shengrui, X.; Yue, H.; Huantao, D.; Jincheng, Z.; Jinfeng, Z.; Xiaowei, Z.; Zhiming, L.; Jinyu, N. Surface morphology of [112¯0]a-plane GaN growth by MOCVD on [11¯02]r-plane sapphire. *J. Semicond.* **2009**, *30*, 043003. [CrossRef]
36. Rajgoli, T.; Hinge, S.; Sant, T.; Jejurikar, S.M.; Mandal, A.; Banpurkar, A.; Rambadey, O.; Sagdeo, P.; Deshpande, U. Nonpolar Growth of GaN Films on Polar Sapphire Substrate Using Pulsed Laser Deposition: Investigation of Substrate Temperature Variation on the Quality of Films. *Phys. Status Solidi B* **2023**, *260*, 2200587. [CrossRef]
37. Wang, C.; Jiang, Y.; Die, J.; Yan, S.; Hu, X.; Hu, W.; Ma, Z.; Deng, Z.; Jia, H.; Chen, H. Improved crystal quality of non-polar *a*-plane GaN epi-layers directly grown on optimized hole-array patterned r-sapphire substrates. *Crystengcomm* **2019**, *21*, 2747–2753. [CrossRef]
38. Darakchieva, V.; Paskova, T.; Schubert, M.; Arwin, H.; Paskov, P.P.; Monemar, B.; Hommel, D.; Heuken, M.; Off, J.; Scholz, F.; et al. Anisotropic strain and phonon deformation potentials in GaN. *Phys. Rev. B* **2007**, *75*, 195217. [CrossRef]
39. Wu, Z.H.; Fischer, A.M.; Ponce, F.A.; Yokogawa, T.; Yoshida, S.; Kato, R. Role of the buffer layer thickness on the formation of basal plane stacking faults in *a*-plane GaN epitaxy on r-sapphire. *Appl. Phys. Lett.* **2008**, *93*, 011901. [CrossRef]
40. Dai, J.N.; Wu, Z.H.; Yu, C.H.; Zhang, Q.; Sun, Y.Q.; Xiong, Y.K.; Han, X.Y.; Tong, L.Z.; He, Q.H.; Ponce, F.A.; et al. Comparative Study on MOCVD Growth of a-Plane GaN Films on r-Plane Sapphire Substrates Using GaN, AlGaN, and AlN Buffer Layers. *J. Electron. Mater.* **2009**, *38*, 1938–1943. [CrossRef]
41. McLaurin, M.B.; Hirai, A.; Young, E.; Wu, F.; Speck, J.S. Basal Plane Stacking-Fault Related Anisotropy in X-ray Rocking Curve Widths ofm-Plane GaN. *Jpn. J. Appl. Phys.* **2008**, *47*, 5429–5431. [CrossRef]
42. Zhao, J.; Zhang, X.; Fan, A.; Chen, S.; He, J.; Pan, J.; Chen, D.; Tian, M.; Feng, Z.C.; Chang, J.; et al. Effects of an in-situ SiN_x interlayer on structural and optical properties for nonpolar *a*-plane GaN epilayers. *Jpn. J. Appl. Phys.* **2020**, *59*, 010909. [CrossRef]
43. Liang, J.; Yang, Y.; Kong, D.; Song, Z.; Wang, W.; Li, G. Low-temperature growth of high-quality *a*-plane GaN epitaxial films on lattice-matched LaAlO3 substrates. *Vacuum* **2020**, *182*, 109687. [CrossRef]
44. Kadleíková, M.; Breza, J.; Veselý, M. Raman spectra of synthetic sapphire. *Microelectron. J.* **2001**, *32*, 955–958. [CrossRef]
45. Gao, H.; Yan, F.; Li, J.; Wang, J.; Yan, J. Polarized Raman scattering studies of nonpolara-plane GaN films grown onr-plane sapphire substrates by MOCVD. *Phys. Status Solidi A* **2006**, *203*, 3788–3792. [CrossRef]
46. Vurgaftman, I.; Meyer, J.R.; Ram-Mohan, L.R. Band parameters for III–V compound semiconductors and their alloys. *J. Appl. Phys.* **2001**, *89*, 5815. [CrossRef]

47. Davydov, V.Y.; Averkiev, N.S.; Goncharuk, I.N.; Nelson, D.K.; Nikitina, I.P.; Polkovnikov, A.S.; Smirnov, A.N.; Jacobson, M.A.; Semchinova, O.K. Raman and photoluminescence studies of biaxial strain in GaN epitaxial layers grown on 6H–SiC. *J. Appl. Phys.* **1997**, *82*, 5097. [CrossRef]
48. Teng, J.; Sheng-Rui, X.; Jin-Cheng, Z.; Zhi-Yu, L.; Ren-Yuan, J.; Yue, H. Growth of a-Plane GaN Films on r-Plane Sapphire by Combining Metal Organic Vapor Phase Epitaxy with the Hydride Vapor Phase Epitaxy. *Chin. Phys. Lett.* **2015**, *32*, 088103.
49. Sun, Q.; Yerino, C.D.; Ko, T.S.; Cho, Y.S.; Lee, I.-H.; Han, J.; Coltrin, M.E. Understanding nonpolar GaN growth through kinetic Wulff plots. *J. Appl. Phys.* **2008**, *104*, 093523. [CrossRef]